Available online at www.sciencedirect.com
SCIENCE DIRECT®
Journal of Computational Physics 199 (2004) 41–65
JOURNAL OF COMPUTATIONAL PHYSICS
www.elsevier.com/locate/jcp

A grid-free dilatation element method for quasi-one-dimensional gas dynamics

Peter S. Bernard *, Jun Shen

Department of Mechanical Engineering, University of Maryland, College Park, MD 20742, USA

Received 26 September 2003; received in revised form 22 January 2004; accepted 29 January 2004
Available online 5 March 2004

Abstract

A grid-free scheme for solving quasi-one-dimensional, isentropic, compressible flow in the subsonic regime is developed with a view toward its eventual generalization to three-dimensional turbulent compressible flow. The computational elements contain information about the dilatation and temperature fields. Velocity is recovered by summing over the contributions of individual elements. Differentiated terms in the governing equations are evaluated using a moving least-square fit with Gaussian weighting function. The transient flow in a suddenly constricted duct is computed including relaxation to an equilibrium solution. An accurate scheme to accommodate the passage of dilatation through the inflow and outflow boundaries is developed using the wave properties of the governing equations. The predicted duct flow matches the exact equilibrium solution and the expected properties of the transient wave field.

PACS: 47.40.Dc; 02.70.Ns

Keywords: Compressible flow; Gridfree; Quasi-one-dimensional flow

1. Introduction

Numerical schemes for predicting compressible turbulent flow parallel the experience with the incompressible case: direct numerical simulations (DNS) are possible and successful at relatively low Reynolds numbers [11,12,14] while modeling is necessary for high speed flows typically encountered in real world applications. Among the modeling possibilities, interest in large eddy simulations (LES) for compressible flow [13] has been rising by virtue of its reduced reliance on modeling in comparison to traditional Reynolds averaged approaches and the opportunities provided by high speed computers. While LES is traditionally practiced through grid-based schemes, it is also possible to formulate LES via the grid-free vortex method

* Corresponding author. Tel.: +1-301-405-5272; fax: +1-301-314-9477.
E-mail address: bernard@umd.edu (P.S. Bernard).

0021-9991/$ - see front matter
doi:10.1016/j.jcp.2004.01.030

[3,4,15,18], and, after suitable generalization to include the effects of compressibility, a grid-free LES for compressible flow can be envisaged.

Motivation for the pursuit of grid-free compressible LES schemes is based on a desire to bring to this case the same advantages intrinsic to incompressible flow. For example: the ability to resolve sharp vortical features without diffusion, natural self-adaptivity and the deployment of novel subgrid stress models (e.g. hairpin removal [5]). Moreover, compressible turbulent flow has been shown to be an important phenomenon in its own right (i.e., not conducive to modeling by mere extension of incompressible flow models). In fact, by their use of Lagrangian elements containing information about the vorticity and dilatation, grid-free schemes provide an opportunity to separately analyze the role of compressibility within turbulent flow conditions. This new perspective has the potential to give direct and unique information about how compressibility affects turbulence.

How best to extend vortex methods to compressible turbulent flow is not self-evident and there have been a number of recent studies that have explored means of accomplishing this. In [9] the volumetric expansion associated with a flame front in a model of a combustion tunnel was modeled using grid-free dilatation elements. The strength and history of the dilatation was tied to the properties of the flame propagation thereby bypassing the need to directly model the dilatation equation. The results are for the most part qualitative and show an affinity with experimental observations. A particle method was also used to study droplet evaporation [20], in which volume sources at the locations of the droplets capture the expansion part of the velocity field produced during the evaporation process.

In recent activity, Strickland [19] considered the general requirements of a grid-free compressible flow solver and tested a specific model on radially and spherically symmetric flows containing disturbances to the vorticity and temperature fields in isentropic conditions. A single set of computational elements contained the vorticity, dilatation and temperature. The wave-like character of the propagating disturbances was computed successfully. An extension of this [17] was used to solve for a radially symmetric swirl flow with initially constant temperature. The velocity was recovered from numerical quadrature of the Helmholtz decomposition. Differentiated terms in the equations of motion were computed using finite differences by taking advantage of the ordering of elements that is possible in one-dimensional calculations.

In [7,8] a method deploying a single set of grid-free elements carrying vorticity, dilatation, enthalpy, entropy, and density was developed. A major focus of this work was the generalization of the particle strength exchange (PSE) method [6] to accommodate all differentiated terms in the equations of motion. As in all such schemes depending on quadrature over a field of irregularly spaced elements, it was necessary to re-mesh periodically. The approach has thus far been applied to computing co-rotating and leapfrogging vortices in compressible flow, with a special interest in computing the associated acoustic field.

This paper presents a scheme for the grid-free representation of quasi-one-dimensional, isentropic, compressible, subsonic flow that is the first step in constructing a grid-free LES of compressible turbulence. In this simpler setting, we wish to develop proven numerical procedures for accommodating the kind of phenomena that will be present in three-dimensions as well as examine the effectiveness of techniques that will be more or less necessary in turbulent flow applications. The method has some similarities with the aforementioned efforts, but differs in a number of aspects so as to be consistent with future extension to 3D turbulent compressible flow. For example, to avoid the inefficiency and numerical diffusion associated with remeshing the present scheme uses local least-square fitting to estimate differentiated terms in the governing equations. Similarly, the velocity field is calculated as the sum of individual contributions from dilatation elements, rather than as a quadrature approximation to the global integral. In addition, we consider as an application, the transient development of quasi-one-dimensional flow in a duct that involves wave phenomena, inlet and outlet boundary conditions and convergence to an equilibrium. This flow is readily generalized to higher dimensions and is relevant to industrial applications.

In the following we first describe the general characteristics of the problem of interest including the basic requirements of the grid-free solution scheme. Next we consider the velocity computation from the field of

dilatation elements and then present the numerical algorithm. The final sections present results of computations of duct flow followed by some conclusions.

2. General considerations

We are concerned with a quasi-one-dimensional model of compressible flow in a variable area duct, as shown in Fig. 1. In this, flow properties are assumed to vary only in the streamwise direction, x, and in time, t. We assume that the variation in the cross-sectional area of the duct, $A(x)$, is relatively small so that the assumption of one-dimensionality is reasonable. Equations expressing mass, momentum and energy conservation for these conditions may be derived from control volume analyses in which the streamwise velocity is taken to be constant on cross-sections [1]. The result for the density ρ is

$$\dot{\rho} = -\rho(\theta + u\alpha), \tag{1}$$

where the notation $\dot{(\,)} \equiv \partial/\partial t + u\,\partial/\partial x$ represents the total (i.e. convective) derivative, u is the velocity, $\theta = \partial u/\partial x$ is the dilatation and $\alpha \equiv (\mathrm{d}A/\mathrm{d}x)/A$ is non-zero only in regions where the duct changes size. A similar consideration of the momentum balance yields

$$\dot{u} = -\frac{1}{\rho}\frac{\partial p}{\partial x}, \tag{2}$$

where p is the pressure.

In view of our intention to use θ as the primary representation of the velocity field, we replace (2) with the corresponding equation for dilatation, namely,

$$\dot{\theta} = -\theta^2 - \frac{\partial}{\partial x}\left(\frac{1}{\rho}\frac{\partial p}{\partial x}\right), \tag{3}$$

derived by taking a spatial derivative. Finally, applying an energy balance yields an equation for the internal energy, e, in the form

$$\dot{e} = -\frac{p}{\rho}(\theta + u\alpha), \tag{4}$$

which becomes an equation for the temperature T after assuming further that $e = c_v T$, where c_v is the specific heat at constant volume. If one adopts a Lagrangian viewpoint such as will be done for this study, then (1)–(4) may be interpreted as governing the properties of the Lagrangian elements as they move through the flow field. In this case, the left-hand sides of the equations are interpreted as simple time derivatives.

For the equilibrium (i.e., non-transient) flow in a duct, mass conservation clearly implies that

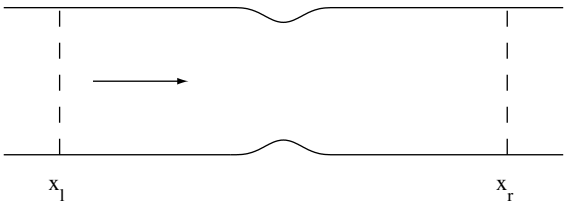

Fig. 1. Geometry of duct flow.

$$\rho u A = Q, \tag{5}$$

where Q is the constant mass flux down the duct. For incompressible flow with constant density a calculation of dilatation based on (5) gives

$$\theta = -u\alpha, \tag{6}$$

which means that despite incompressibility, the assumption of one-dimensionality implies that the dilatation is non-zero in regions where the duct changes area. Note that according to (6), (4) is fully consistent with the constancy of e in isothermal, incompressible flow. Departures of θ from (6) will give an indication (besides changes in ρ and T) of the degree to which the flow is truly compressible.

The dynamical description of the flow is completed with an equation of state, which we take to be the perfect gas law

$$p = \rho R T, \tag{7}$$

with R the gas constant. Without sacrifice of the essential complexity of the calculation we further assume isentropic conditions so that

$$\frac{p}{p_0} = \left(\frac{\rho}{\rho_0}\right)^{\gamma}, \tag{8}$$

where p_0 and ρ_0 refer to upstream equilibrium conditions and $\gamma \equiv c_p/c_v$ is the (assumed constant) ratio of specific heats. Here and henceforth ρ, p and T are assumed to be scaled with their upstream, equilibrium values, so that in such locales $\rho = 1$, $p = 1$ and $T = 1$ where temperature is scaled by T_0. Lengths are scaled by $L = \sqrt{A_0}$ with A_0 denoting the duct area in the upstream, constant region, so that the scaled area $A(x) = 1$ away from the contraction. It is also convenient to choose the velocity scale as the equilibrium sound speed $c_0 = \sqrt{\gamma R T_0}$ so that u, after scaling, is a Mach number. With these choices, time is scaled by L/c_0.

With the aid of (7) and (8), the governing equations can be simplified to a system for just θ and T. After non-dimensionalization, these become

$$\dot{\theta} = -\theta^2 - \frac{1}{\gamma - 1}\frac{\partial^2 T}{\partial x^2}, \tag{9}$$

and

$$\dot{T} = -(\gamma - 1)T(\theta + u\alpha). \tag{10}$$

Coupled to these are additional relations representing the movement and distortion of the computational elements. Assuming that a typical element has length $h(t)$ and center $X(t)$, then the path of the element satisfies

$$\dot{X} = u, \tag{11}$$

where u is evaluated at X at time t. Furthermore, it may be shown that, approximately,

$$\dot{h} = h\theta, \tag{12}$$

with exact equality following in the limit as $h \to 0$. It is assumed throughout this work that h is sufficiently small so that (12) holds with acceptable accuracy.

It may be remarked that as an alternative to separately tracking X and h, one can instead calculate the movement of the endpoints of elements since this gives the same information. Though this approach may

potentially offer more accuracy, it is not pursued here since it cannot be practically implemented in higher dimensions. In contrast, (12) has a straightforward analogy in two and three dimensions.

The complete numerical description of the flow field consists of N elements at locations X_i with lengths h_i and flow properties θ_i and T_i, where $i = 1, \ldots, N$. These are contained in the computational domain $x_l \leqslant x \leqslant x_r$ where it is assumed for simplicity that x_l and x_r are sufficiently far upstream and downstream of the constriction, respectively, so that $A(x) = 1$ in their vicinity. This assumption allows for a relatively straightforward modeling of inflow and outflow boundary conditions, as will be seen below. Another simplifying step is to initiate the calculation with elements covering the complete flow domain and to introduce new elements at the inflow, as necessary, so as to maintain full coverage for all time. Such an approach is not strictly required, since elements are not needed in regions where $\theta = 0$ and $T = 1$. However, the modest cost of one-dimensional computations is such that there is little incentive to pursue cost saving strategies in which only the minimal number of elements is kept at any one time. In higher dimensions the advantage of eliminating unnecessary elements is greater and it may be anticipated that generalization of the present scheme to such flows will include a capability for omitting dilatation-free elements.

For most of our computations $h_i, i = 1, \ldots, N$ are initially chosen to be equal, though this property is not generally retained as time proceeds. Some test calculations have also been performed with randomly chosen values of h_i to better mimic conditions expected in higher dimensions, especially when turbulence is present. This modification is found to have minimal effect on the results, as will be demonstrated below.

3. Velocity evaluation

Velocity is computed by summing the contributions from individual dilatation elements in analogy to the approach that would naturally be pursued in higher dimensions. Thus, consistent with having dilatation θ_i and size h_i, the ith element produces the velocity field

$$\Phi_i(x) = \begin{cases} -h_i\theta_i/2 & x \leqslant X_i - h_i/2, \\ \theta_i(x - X_i) & |x - X_i| < h_i/2, \\ h_i\theta_i/2 & x \geqslant X_i + h_i/2, \end{cases} \tag{13}$$

that is illustrated in Fig. 2. Clearly, θ_i is assumed to be distributed uniformly over the element. The total velocity field at x is a sum of contributions from all elements and takes the form

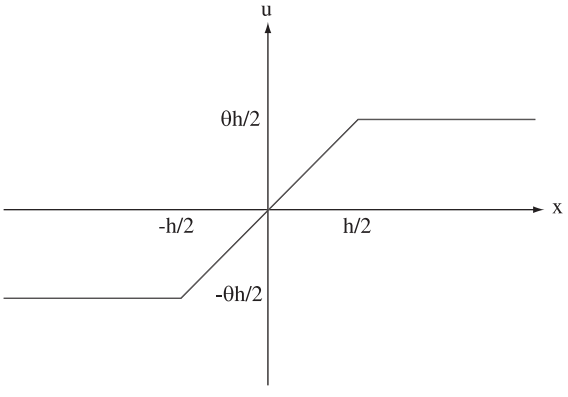

Fig. 2. Velocity contributed by a dilatation element.

$$u(x) = C + \sum_{i=1}^{N} \Phi_i(x), \tag{14}$$

where the constant C represents a one-dimensional potential flow used to satisfy boundary conditions.

Eq. (14) needs to satisfy the far field condition $u(-\infty) = u_0$ in which case after solving for C using (13) and back substituting, (14) becomes

$$u(x) = u_0 + \sum_{i=1}^{N} (\Phi_i(x) + h_i\theta_i/2). \tag{15}$$

For the isentropic flow considered here, it is also the case that $u(+\infty) = u_0$ since the duct has the same uniform area both upstream and downstream of the constriction. This yields from (15) the consistency condition

$$\sum_{i=1}^{N} h_i\theta_i = 0, \tag{16}$$

which is just a numerical approximation to the identity

$$\int_{-\infty}^{\infty} \theta(x)\mathrm{d}x = 0. \tag{17}$$

There is nothing in the argument leading to (14) that limits the sum in that equation to dilatation elements lying in the region of interest between $x = x_\mathrm{l}$ and $x = x_\mathrm{r}$. In fact, all elements containing non-zero dilatation must be included in that relation. In particular, as will be seen below, during the transient development of the duct flow, waves carry θ out toward $x = \pm\infty$ from the contraction. Thus, despite our interest in the flow in the computational region only, it is still necessary to take into account the presence of dilatation outside the computational domain. This must be done without explicitly providing elements to keep track of this part of the dilatation field since otherwise there would be no end to the extent of the computational domain. This problem is similar in principle to that faced in vortex methods when vorticity lying outside the region of interest must nevertheless be accounted for when determining the velocity field [2].

In this study we use the wave properties of the governing equations to help recover the effect of dilatation that passes outside the computational domain. This is done in such a way that outward moving waves pass through the boundaries without reflecting unphysical waves back into the computational domain. This approach may be contrasted, for example, with that in [7] where a special class of boundary elements is introduced in order to accomplish a similar objective.

For x limited to the computational region (i.e., $x_\mathrm{l} \leqslant x \leqslant x_\mathrm{r}$), it is evident that all elements for which $x_i > x_\mathrm{r}$ make no contribution to the sum in (15) (since $\Phi_i(x) + h_i\theta_i/2 = 0$ in such cases). Moreover, the contribution of elements for which $x_i < x_\mathrm{l}$ can be combined together into a term approximating

$$\Delta_\mathrm{l} \equiv \int_{-\infty}^{x_\mathrm{l}} \theta(x)\mathrm{d}x, \tag{18}$$

thereby yielding the result

$$u(x) = u_0 + \Delta_\mathrm{l} + \sum_{i=1}^{N} (\Phi_i(x) + h_i\theta_i/2), \tag{19}$$

where it is to be understood here and henceforth that the summation in (19) is only over the elements lying within the computational domain, and x satisfies $x_l \leqslant x \leqslant x_r$. Defining,

$$\Delta_r \equiv \int_{x_r}^{\infty} \theta(x)\mathrm{d}x, \tag{20}$$

according to (16) and (17)

$$\Delta_l + \sum_{i=1}^{N} h_i\theta_i + \Delta_r = 0, \tag{21}$$

in which case (19) can be rearranged as

$$u(x) = u_0 + \frac{1}{2}\Delta_l + \sum_{i=1}^{N} \Phi_i(x) - \frac{1}{2}\Delta_r, \tag{22}$$

which is the velocity relation that will be used in this study. Δ_l and Δ_r depend only on θ outside the computational domain, and in fact are related to the velocities at the left and right boundaries, respectively, through the identities

$$u_l \equiv u(x_l) = u_0 + \Delta_l \tag{23}$$

and

$$u_r \equiv u(x_r) = u_0 - \Delta_r. \tag{24}$$

These relations may be derived from either (18) and (20) or (21) and (22). For (22) to be useful in determining velocities in the numerical scheme, the changes of Δ_l and Δ_r in time must be determined over the course of the flow evolution. In fact, this information can be found using the wave structure of the equations as will be shown below in the course of our presentation of the algorithm.

4. Numerical algorithm

For the flows of interest in this study a Lagrangian particle method can only get the end steady state solution as the result of computing the time accurate (i.e., physical) transient solution. For the present work the initial state is generally taken to be the uniform conditions $u_i^0 = u_0$, $T_i^0 = 1$, and $\theta_i^0 = 0$ for $i = 1, \ldots, N$ where the superscript denotes the time step of the calculation. Typically $h_i^0 = \overline{h}$ where $\overline{h} \equiv (x_r - x_l)/N$ and $X_i = (i - 0.5)\overline{h}, i = 1, \ldots, N$ except when variable h_i are prescribed. Conceptually the problem of interest may be viewed as an initially constant area duct with uniform flow that is suddenly indented to the shape given by $A(x)$ at time 0.

For convenience in this discussion it will be assumed that the element closest to the inlet has $i = 1$ while the one nearest the outlet has $i = N$. At the start of any time integration step that brings the solution from $t_n = n\,\mathrm{d}t$ to $t_{n+1} = (n+1)\mathrm{d}t$, X_i^n, θ_i^n, T_i^n and h_i^n, $i = 1, \ldots, N$ are known and such that they are located entirely within the computational domain. It is also assumed that the respective ends of elements 1 and N are aligned flush with the inlet and outlet boundaries (i.e., the conditions $x_l = X_1 - h_1/2$ and $x_r = X_N + h_N/2$ are satisfied). In fact, these last conditions are always true since they will be forced to be satisfied at the end of each time step. It is also assumed, for reasons to become clear momentarily, that boundary values of velocity and temperature are computed and saved at every time step. These are denoted by u_l^n and u_r^n for the velocities at the left and right boundaries at time t_n, respectively, and similarly for T_l^n and T_r^n. Finally, it is assumed that Δ_l^n and Δ_r^n are known at the start of each time step.

Time advancement is achieved via a second order Runge–Kutta scheme applied to (9)–(12). A fourth order Runge–Kutta algorithm was also tested and yielded similar outcomes. The Lagrangian nature of the method combined with the use of θ as a primary variable leads to some technical complexity in the implementation of boundary conditions. To simplify this discussion it proves to be advantageous to present in sequence the steps in the algorithm that advance the solution for one time step.

4.1. First Runge–Kutta step

At the outset note that any numerical procedure for solving (9)–(12) requires evaluation of α_i^n, u_i^n and $\partial^2 T_i^n/\partial x^2$. Among these, $\alpha_i^n, i = 1, \ldots, N$ are computed straightforwardly from the properties of $A(x)$ at the positions X_i. $u_i^n, i = 1, \ldots, N$ are readily computed from (22) using the information available at time t_n. The calculation of $\partial^2 T_i^n/\partial x^2$ poses some problems. In this work it is computed using a local weighted least-square fit of a fourth degree polynomial that is determined according to the collection of elements lying in a local domain $|x - X_i| \leqslant l$, where the distance l is a parameter that needs to be specified. The Gaussian weighting function

$$w(x - X_i) = \mathrm{e}^{-(x-X_i)^2/\sigma^2} \tag{25}$$

with parameter σ^2 is used in the least-square fit. The choice $\sigma^2 = l^2/10$ has been found through numerical experimentation to be acceptable. For the most part l is taken to be the same for all elements without regard to their position. We also do not vary l with N, so the number of elements that fall within the local least-square window is not forced to be the same for all calculations. A similar least-square approach was used by Marshall and Grant [16] in a vortex method calculation of axisymmetric flows with and without swirl. In that study a quadratic polynomial was used and the scale of the Gaussian weight function depended on the particle spacing. For the present application the latter approach generally led to instability, particularly for the higher range of u_0. This may be attributable, in part, to the use of quadratic polynomials that are increasingly unable to accurately resolve the sharp features of T and its second derivative that appear as u_0 increases. In fact, for large u_0 it was found that stability requires that the least-square fit be over a window of a minimal size and N must be relatively large. These conditions cannot be satisfied if the window size scales with the particle size. It is also noteworthy that the least-square fit tends to cause instabilities in the computed fields if uniform weighting is used in place of (25). One exception is that a smooth transition from (25) to uniform weighting proves to be beneficial in permitting waves to pass smoothly through the outflow boundary. The change in form from Gaussian to uniform weighting is done via a homotopy beginning at the distance l from the outflow boundary.

For elements close to the inlet and outlet a complete set of data with which to make the least-square fits is not available from the elements lying in the computational domain. To get a collection of symmetrically placed data for fits at these locations it is necessary to use data outside the computational domain. In fact, a means of acquiring such data is offered by the wave structure of solutions near the inlet and outlet where $A(x) = 1$ so standard results apply from the one-dimensional gas dynamics equations. In particular, the hyperbolic system of equations for u and T that may be derived from (2) and (10) (after eliminating p and ρ) has right and left traveling characteristic families, x^+ and x^-, respectively, determined as the solution to

$$\frac{\mathrm{d}x^+}{\mathrm{d}t} = u + \sqrt{T} \tag{26}$$

and

$$\frac{\mathrm{d}x^-}{\mathrm{d}t} = u - \sqrt{T}, \tag{27}$$

where $\sqrt{T}$ is equivalent to the sound speed c in the present scaling. The Riemann invariant

$$R^+ \equiv \frac{u}{2} + \frac{\sqrt{T}}{\gamma - 1} \tag{28}$$

is constant on lines given by (26) while

$$R^- \equiv \frac{u}{2} - \frac{\sqrt{T}}{\gamma - 1} \tag{29}$$

is constant on (27).

In the vicinity of $x = x_r$, the characteristics moving toward the duct contraction (i.e., in the negative x direction) are in the x^- family. Each of these originate in a region with velocity u_0 and temperature 1, so they have the same value of R^-, namely, $u_0/2 - 1/(\gamma - 1)$. This means that u and T in this region are related via

$$\frac{u}{2} - \frac{\sqrt{T}}{\gamma - 1} = \frac{u_0}{2} - \frac{1}{\gamma - 1}, \tag{30}$$

a formula that supplies a means of obtaining T_r once u_r is computed from (24). In fact,

$$T_r = (1 + (u_r - u_0)(\gamma - 1)/2)^2. \tag{31}$$

The fact that R^+ is constant along right moving characteristics proceeding away from the contraction, together with the validity of (30) in this region implies that u and T are constants on the x^+ lines leaving from x_r at any given time. These lines are therefore straight with slope given by $u_r + \sqrt{T_r}$ and they provide a means for recreating the T distribution for $x > x_r$ for purposes of supplying the data needed for the least square fit of T used in computing $\partial^2 T_i^n/\partial x^2$. The procedure is illustrated in Fig. 3 where it is seen that the x^+ family of lines originating at x_r at earlier times $t_{n-1}, t_{n-2}, \ldots$ and so forth are extended forward in time until t_n, where they occupy locations $x_r^{n,k} \equiv x_r + (n-k)\mathrm{d}t(u_r^k + \sqrt{T_r^k}), k = n, (n-1), \ldots$ and have temperatures T_r^k. For a typical $\mathrm{d}t$ used in the simulations the points $x_r^{n,k}$ are much more closely spaced than the dilatation elements, so the actual data needed for the least-square fits is obtained from the data pairs $(x_r^{n,k}, T_r^k)$ by interpolation over points spaced by $\overline{h}$.

Without giving the details it may be shown that similar considerations apply to obtaining temperature data ahead of the inlet boundary. In this case, analogously to (31) there is

$$T_l = (1 - (u_l - u_0)(\gamma - 1)/2)^2, \tag{32}$$

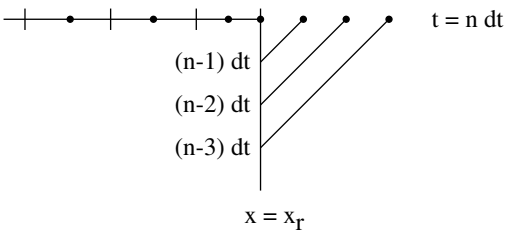

Fig. 3. Filled circles denote the locations of T values that form the basis for a least-square fit of T near the outflow boundary. Characteristic lines emanating from $x = x_r$ at times preceding t_n are shown as diagonal lines.

a relation that may be used after u_l is first computed from (23). Moreover, the least-square fit of T at points near $x = x_l$ is aided by data obtained by interpolation from temperatures T_l^k associated with the locations $x_l^{n,k} \equiv x_l + (n-k)\mathrm{d}t(u_l^k - \sqrt{T_l^k}), k = n, (n-1), \ldots$ Finally, it should be noted that during the startup phase of the calculation, before disturbances created by the constriction reach the boundaries, it is assumed that $u_l^k = u_r^k = u_0$ and $T_l^k = T_r^k = 1$ for $k = 0, -1, -2, \ldots$ to as early a time as is necessary for the least-square fit.

Once $\partial^2 T_i^n/\partial x^2$ is computed, the solution to (9)–(12) can be advanced through the first step of a second order Runge–Kutta scheme given by

$$X_i^* = X_i^n + \mathrm{d}t\, u_i^n, \tag{33}$$

$$\theta_i^* = \theta_i^n - \mathrm{d}t\left((\theta_i^n)^2 + \frac{1}{\gamma - 1}\frac{\partial^2 T_i^n}{\partial x^2}\right), \tag{34}$$

$$T_i^* = T_i^n - \mathrm{d}t(\gamma - 1)T_i^n\left(\theta_i^n + u_i^n \alpha_i^n\right), \tag{35}$$

$$h_i^* = h_i^n + \mathrm{d}t\, h_i^n \theta_i^n, \tag{36}$$

yielding the provisional values, X_i^*, θ_i^*, T_i^* and $h_i^*, i = 1, \ldots, N$ for the solution at $t + \mathrm{d}t$.

4.2. Second Runge–Kutta step

As part of the second step of the Runge–Kutta scheme it is necessary to evaluate u_i^*, α_i^* and $\partial^2 T_i^*/\partial x^2$ using the provisional solution obtained from (33)–(36). As before, computing α_i^* is straightforward using the values of X_i^*. In addition, $\partial^2 T_i^*/\partial x^2$ may be computed using the least-square approach applied to the data points (X_i^*, T_i^*). Near the boundary this data is supplemented by information about T outside the domain that is reconstructed from the local wave structure. In particular, as depicted in Fig. 4 for the outlet boundary, T values can be established at locations determined by the characteristics departing from x_l and x_r at earlier times and extended until t_{n+1}.

The computation of u_i^* from (22) can be done once Δ_l^* and Δ_r^* are computed. The later calculation must be sensitive to the effect of the motion of the elements and characteristics that has taken place during the first step of the Runge–Kutta scheme. Two observations need to be made:

(1) While Δ_r^n, for example, represents the integral of θ over the region $x \geqslant x_r$ at t_n, it also represents the integral of θ over the region $x \geqslant x_r + \mathrm{d}t(u_r^n + \sqrt{T_r^n})$ at time t_{n+1}. This follows from the constancy of u on the right moving characteristics leaving from x_r and the definitions in (20) and (24). A similar observation

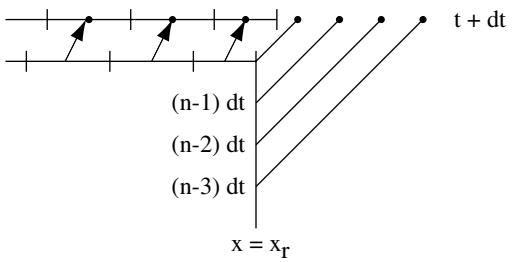

Fig. 4. Filled circles denote the locations of T values forming the basis for a least-square fit of T near the outflow boundary at the start of the second step of the Runge–Kutta scheme. Movement of the dilatation elements to positions X_i^* is also indicated.

applies at the left boundary: thus Δ_{l}^n represents the integral of θ in $x \leqslant x_{\mathrm{l}}$ at t_n and also $x \leqslant x_{\mathrm{l}} + \mathrm{d}t(u_{\mathrm{l}}^n - \sqrt{T_{\mathrm{l}}^n})$ at time t_{n+1}.

(2) The computational elements are no longer flush with x_{l} and x_{r} after the first Runge–Kutta step. In particular, the Nth element now lies so that it extends past the boundary at x_{r} (i.e. $X_N^* + h_N^*/2 > x_{\mathrm{r}}$) as seen in Fig. 5. Similarly, a gap has formed between x_{l} and $X_1^* - h_1^*/2$.

A simple way of proceeding at this point is to recognize that the formalism leading to (22)–(24) is equally valid if it is applied to a temporary computational domain encompassing the left and rightmost points of the dilatation elements at positions X_i^*. In this scheme, quantities Δ_{l}^* and Δ_{r}^* are required that provide for dilatation lying in $x \leqslant X_1^* - h_1^*/2$ and $x \geqslant X_N^* + h_N^*/2$, respectively, at time t_{n+1}. In view of the first observation above, these quantities are readily computed from Δ_{l} and Δ_{r}, by adding appropriate corrections that approximate $\int \theta \,\mathrm{d}x$ over the gap regions that form between $X_N^* + h_N^*/2$ and $x_{\mathrm{r}} + \mathrm{d}t(u_{\mathrm{r}}^n + \sqrt{T_{\mathrm{r}}^n})$ at the outflow boundary and $x_{\mathrm{l}} + \mathrm{d}t(u_{\mathrm{l}}^n - \sqrt{T_{\mathrm{l}}^n})$ and $X_1^* - h_1^*/2$ at the inflow boundary. The situation at the outlet is illustrated in Fig. 5. Since we want Δ_{r}^* to equal $\int \theta \,\mathrm{d}x$ for $x \geqslant X_N^* + h_N^*/2$, it is clear that an approximation to this is

$$\Delta_{\mathrm{r}}^* = \Delta_{\mathrm{r}}^n + (\mathrm{d}t\sqrt{T_{\mathrm{r}}^n})\theta^*|_{x=(x_{\mathrm{r}}+u_{\mathrm{r}}^n\,\mathrm{d}t+\sqrt{T_{\mathrm{r}}^n}\,\mathrm{d}t/2)}, \tag{37}$$

where $\sqrt{T_{\mathrm{r}}^n}\,\mathrm{d}t$ is the size of the gap between the end of the Nth element and the characteristic that left from x_{r} at time t_n. A similar consideration yields the relation

$$\Delta_{\mathrm{l}}^* = \Delta_{\mathrm{l}}^n + (\mathrm{d}t\sqrt{T_{\mathrm{l}}^n})\theta^*|_{x=(x_{\mathrm{l}}+u_{\mathrm{l}}^n\,\mathrm{d}t-\sqrt{T_{\mathrm{l}}^n}\,\mathrm{d}t/2)} \tag{38}$$

at the left boundary. The required values of θ^* in (37) and (38) are found via interpolation using the set of θ_i^* at X_i^* together with θ values outside the computational domain. The latter are easily computed from the simple finite difference approximations

$$\theta_{\mathrm{l}}^{n+1,k} \approx \frac{u_{\mathrm{l}}^k - u_{\mathrm{l}}^{k-1}}{\Delta x_{\mathrm{l}}^{n+1,k}} \tag{39}$$

and

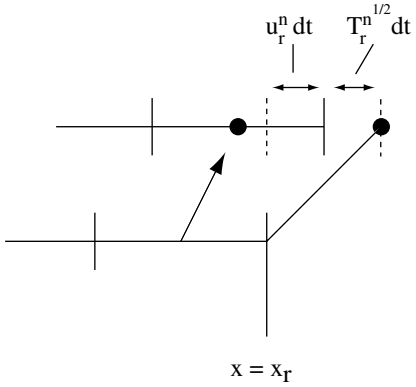

Fig. 5. The Nth element has moved past x_{r} a distance given approximately by $u_{\mathrm{r}}^n\,\mathrm{d}t$. The characteristic departing from x_{r} arrives at $x_{\mathrm{r}} + \mathrm{d}t(u_{\mathrm{r}}^n + \sqrt{T_{\mathrm{r}}^n})$ after time $\mathrm{d}t$.

$$\theta_{\mathrm{r}}^{n+1,k} \approx \frac{u_{\mathrm{r}}^{k-1} - u_{\mathrm{r}}^{k}}{\Delta x_{\mathrm{r}}^{n+1,k}} \tag{40}$$

for $k = n, n-1, \ldots$ where $\Delta x_{\mathrm{l}}^{n+1,k} \equiv x_{\mathrm{l}}^{n+1,k} - x_{\mathrm{l}}^{n+1,k-1}$ and $\Delta x_{\mathrm{r}}^{n+1,k} \equiv x_{\mathrm{r}}^{n+1,k-1} - x_{\mathrm{r}}^{n+1,k}$. Eq. (39) applies at the points $x_{\mathrm{l}}^{n+1,k} + \Delta x_{\mathrm{l}}^{n+1,k}/2$ while (40) is at the points $x_{\mathrm{r}}^{n+1,k} + \Delta x_{\mathrm{r}}^{n+1,k}/2$. The accuracy of these approximations is aided by the small magnitudes of $\Delta x_{\mathrm{l}}^{n+1,k}$ and $\Delta x_{\mathrm{r}}^{n+1,k}$.

Using Δ_{l}^{*} and Δ_{r}^{*} computed from (37) and (38) in a formula similar to (22) gives a means of computing u_i^{*}. Now all is ready to effect the second step of the Runge–Kutta algorithm:

$$x_i^{n+1} = x_i^{n} + \mathrm{d}t(u_i^{n} + u_i^{*})/2, \tag{41}$$

$$\theta_i^{n+1} = \theta_i^{n} - \mathrm{d}t\left[((\theta_i^{n})^2 + (\theta_i^{*})^2)/2 + \frac{1}{\gamma - 1}\left(\frac{\partial^2 T_i^{n}}{\partial x^2} + \frac{\partial^2 T_i^{*}}{\partial x^2}\right)\Big/ 2\right], \tag{42}$$

$$T_i^{n+1} = T_i^{n} - \mathrm{d}t(\gamma - 1)(T_i^{n}\left(\theta_i^{n} + u_i^{n}\alpha_i^{n}\right) + T_i^{*}\left(\theta_i^{*} + u_i^{*}\alpha_i^{*}\right))/2, \tag{43}$$

$$h_i^{n+1} = h_i^{n} + \mathrm{d}t(h_i^{n}\theta_i^{n} + h_i^{*}\theta_i^{*})/2, \tag{44}$$

that produces the solution at t_{n+1}.

4.3. Boundary conditions

The completion of the time integration step consists of determining $\Delta_{\mathrm{l}}^{n+1}$ and $\Delta_{\mathrm{r}}^{n+1}$, enforcing boundary conditions and adjusting the length and positions of the elements closest to the inlet and outlet so they are flush with the boundaries. The first of these tasks parallels our previous approach to computing Δ_{l}^{*} and Δ_{r}^{*}, only this time the assumption is in effect that the ends of elements 1 and N are exactly at x_{l} and x_{r}, respectively, since they will be so by the end of the time step. According to our first observation above, $\Delta_{\mathrm{l}}^{n+1}$ and $\Delta_{\mathrm{r}}^{n+1}$ are computed by adding to Δ_{l}^{n} and Δ_{r}^{n}, respectively, the amount of θ filling the region between the boundaries and the characteristics that moved out during the interval $\mathrm{d}t$. Using interpolation the following approximations are then suggested:

$$\Delta_{\mathrm{l}}^{n+1} = \Delta_{\mathrm{l}}^{n} + (\mathrm{d}t\sqrt{T_{\mathrm{l}}^{n}})\theta^{n+1}|_{x=(x_{\mathrm{l}}+u_{\mathrm{l}}^{n}\,\mathrm{d}t-\sqrt{T_{\mathrm{l}}^{n}}\,\mathrm{d}t/2)} - (\mathrm{d}t\,u_{\mathrm{l}}^{n})\theta^{n+1}|_{x=(x_{\mathrm{l}}+u_{\mathrm{l}}^{n}\,\mathrm{d}t/2)} \tag{45}$$

and

$$\Delta_{\mathrm{r}}^{n+1} = \Delta_{\mathrm{r}}^{n} + (\mathrm{d}t\sqrt{T_{\mathrm{r}}^{n}})\theta^{n+1}|_{x=(x_{\mathrm{r}}+u_{\mathrm{r}}^{n}\,\mathrm{d}t+\sqrt{T_{\mathrm{r}}^{n}}\,\mathrm{d}t/2)} + (\mathrm{d}t\,u_{\mathrm{r}}^{n})\theta^{n+1}|_{x=(x_{\mathrm{r}}+u_{\mathrm{r}}^{n}\,\mathrm{d}t/2)}. \tag{46}$$

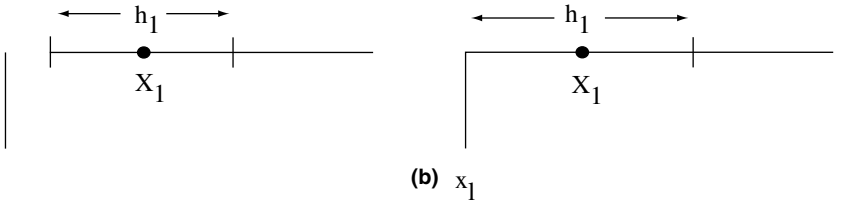

Fig. 6. At each time step the element closest to the inlet is lengthened so that its leftmost point is at the inlet: (a) after element moves, (b) revised element.

It now follows that u_{l}^{n+1} and u_{r}^{n+1} can be obtained from (23) and (24), respectively, while T_{r}^{n+1} and T_{l}^{n+1} are computed from (31) and (32).

The simple adjustments of X_{l}^{n+1} and h_{l}^{n+1} illustrated in Fig. 6 are done to enforce the condition $X_{\mathrm{l}} - h_{\mathrm{l}}/2 = x_{\mathrm{l}}$. This then necessitates slight modification to T_{l}^{n+1} and $\theta_{\mathrm{l}}^{n+1}$ so that they correspond to the new position of the element center. The former is found from cubic interpolation over the updated temperature field. $\theta_{\mathrm{l}}^{n+1}$ on the other hand is calculated in such a way as to preserve the total integrated dilatation within the region between x_{l} and $X_{\mathrm{l}} + h_{\mathrm{l}}/2$. This leads to the equation

$$[\theta_{\mathrm{l}}^{n+1} h_{\mathrm{l}}^{n+1}]_{\mathrm{new}} = [\theta_{\mathrm{l}}^{n+1} h_{\mathrm{l}}^{n+1}]_{\mathrm{old}} + (u_{\mathrm{l}}^{n}\,\mathrm{d}t)\theta^{n+1}|_{x=(x_{\mathrm{l}}+u_{\mathrm{l}}^{n}\,\mathrm{d}t/2)}, \tag{47}$$

which is solved for $\theta_{\mathrm{l}}^{n+1}$ on the left-hand side. The second term on the right-hand side accounts for dilatation in the gap created by the first element moving to the right.

At the outlet boundary an opposite procedure is performed. Here, element N is truncated so that its downstream end is at x_{r}. X_N^{n+1} and h_N^{n+1} are modified in an obvious way. T_N^{n+1} is found by interpolation, while similar to (47) the velocity difference across the Nth element is maintained before and after adjustment via the relation

$$[\theta_N^{n+1} h_N^{n+1}]_{\mathrm{new}} = [\theta_N^{n+1} h_N^{n+1}]_{\mathrm{old}} - (u_{\mathrm{r}}^{n}\,\mathrm{d}t)\theta^{n+1}|_{x=(x_{\mathrm{r}}+u_{\mathrm{r}}^{n}\,\mathrm{d}t/2)}, \tag{48}$$

which is once again used to get θ_N^{n+1} on the left-hand side. The use of (47) and (48) or equivalent appears to be necessary. For example, determining the updated θ by interpolation in this instance can lead to unacceptable oscillations in the solution.

Since the element at the inlet boundary grows slightly in length after each time step it is necessary to periodically subdivide it when it increases beyond a given length. Similarly, the element at the outlet shrinks after each time step and it must occasionally be merged with its nearest neighbor when it is too short. The performance of the algorithm proves to be for the most part insensitive to the exact criterion used to determine when it is time for subdivision and merger. In typical runs, the maximum length of an element is taken to be $3/2\overline{h}$, while the minimum length is $\overline{h}/2$. After element merger or division the position, length, temperature and dilatation of the new elements are determined very much the same way they are during the boundary adjustment at each time step. At this point the integration step is complete and the calculation of a new time step can be initiated.

5. Duct flow

For purposes of illustrating the performance of the numerical algorithm, flow in a quasi-one-dimensional duct with area

$$A(x) = \begin{cases} [1 - \beta/4\{\cos(\pi(1+2x)) - 1\}^2]^2 & |x| \leqslant 0.5, \\ 1 & |x| > 0.5 \end{cases} \tag{49}$$

is computed. The maximum constriction is $(1-\beta)^2$ occurring at $x = 0$. For the results here the parameter $\beta = 0.05$, so the minimum of $A(x)$ is 0.9025. This is a relatively small constriction; for example, $\beta = 0.1$ for the duct in Fig. 1. For most calculations $x_{\mathrm{l}} = -1$ and $x_{\mathrm{r}} = 1$.

It is a simple matter to find the steady state solution corresponding to (49). In fact, for an Eulerian frame of reference in steady flow, (2) and (10) yield the coupled ordinary differential equations

$$\frac{\mathrm{d}u}{\mathrm{d}x} = -\alpha \frac{Tu}{T - u^2}, \tag{50}$$

$$\frac{\mathrm{d}T}{\mathrm{d}x} = (\gamma - 1)\alpha \frac{Tu^2}{T - u^2}, \tag{51}$$

that may be solved for u and T (e.g., using Matlab). For any given upstream condition the local Mach number $M = u/\sqrt{T}$ peaks at the throat except when the downstream flow is supersonic. For the geometry given by (49) with $\beta = 0.05$, $M = 1$ first appears at the throat when $u_0 \approx 0.681$. This then is an upper limit to what we may choose for u_0 if, as is the case here, we want to confine our attention strictly to the subsonic regime.

We use the steady state solution computed from (50) and (51) to test the accuracy of the solution of the grid-free scheme after its passage from the initial state through a transient to an equilibrium flow condition. Since we are proposing a Lagrangian method, the individual computational elements are not in equilibrium. Rather, equilibrium is achieved when each individual element traveling through the computational domain undergoes a similar history. It will suffice here, however, to observe that equilibrium exists for all practical purposes when the plots of velocity, temperature and other fields do not visibly change in time. Since we take constant properties equal to those in the far field as initial conditions, there is always a significant non-steady regime to be crossed. Moreover, even if the equilibrium values of T and u are initially prescribed on elements covering the domain, there remains no obvious means of assigning an equilibrium distribution for h, so this quantity will still have to evolve in time for a complete equilibrium to be reached.

Figs. 7 and 8 present the transient behavior of T and u, respectively, for the flow with $u_0 = 0.5$, $N = 600$, $l = 0.075$ and $\mathrm{d}t = 0.0005$. These results are independent of N so long as it is not so small as to prevent

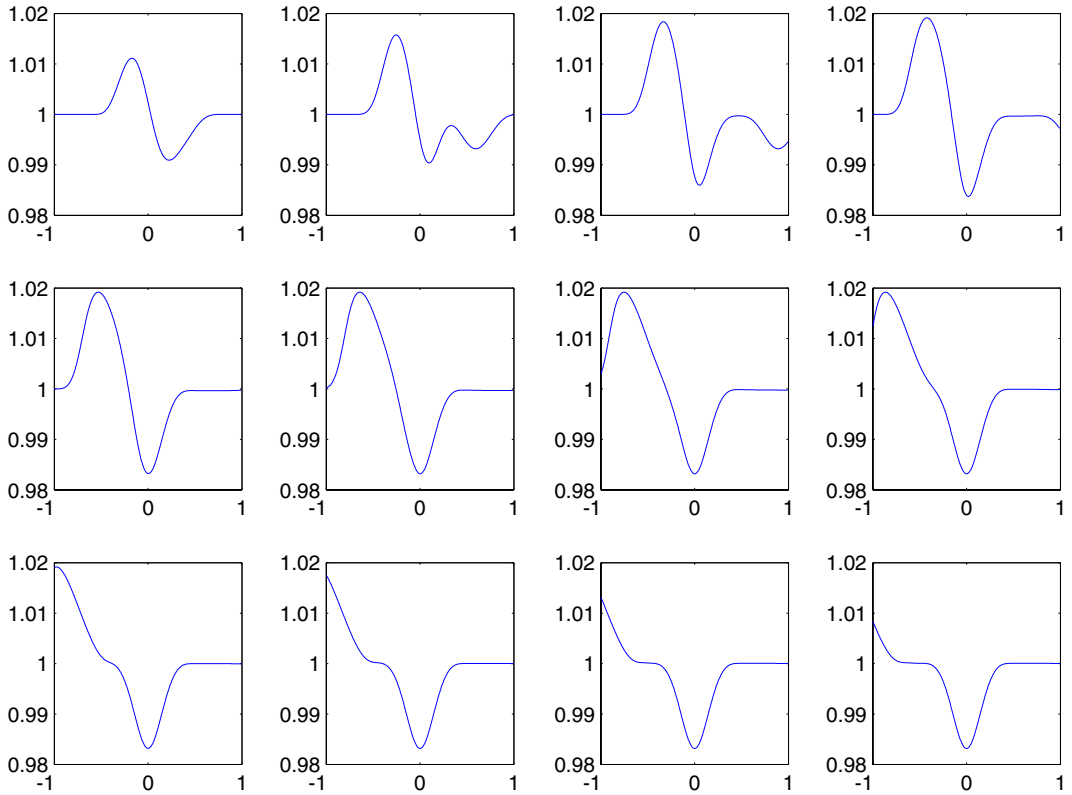

Fig. 7. T in increments of 0.2 from $t = 0.2$ to 2.4 (left to right and top to bottom) for $u_0 = 0.5$ solution.

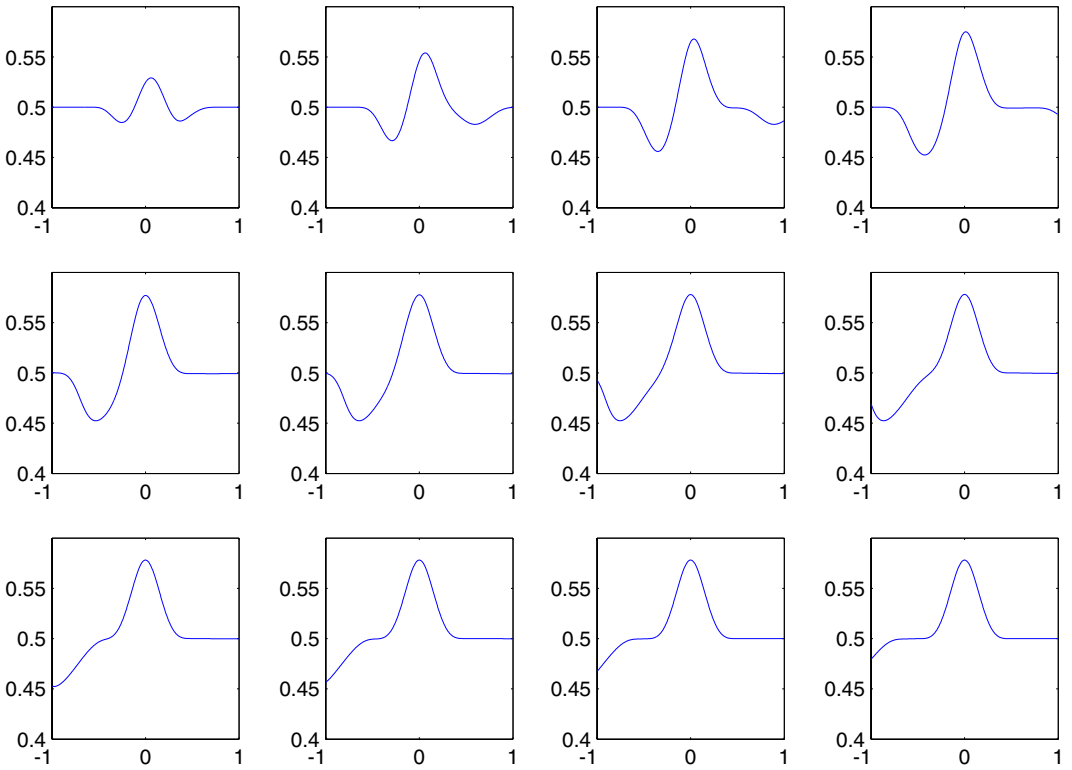

Fig. 8. u in increments of 0.2 from $t = 0.2$ to 2.4 (left to right and top to bottom) for $u_0 = 0.5$ solution.

adequate resolution of the spatial variation in the computed fields, most notably $\partial^2 T/\partial x^2$ as will be seen subsequently. For large dt the method is unstable, but when dt is sufficiently small (e.g., so as to satisfy a CFL type condition) the solutions are independent of this parameter. Fig. 7 shows the development of downstream and upstream traveling waves that originate in the nozzle region. The downstream wave moves with a speed consistent with the right moving characteristics given by (26) while the upstream wave is consistent with (27). Thus, as is evident in the figures, the downstream wave passes through x_r by $t \approx 1$ while the upstream traveling wave passes through x_l by $t \approx 2.4$. Both of the waves cleanly progress through the boundary without noticeable distortion or reflection. In the downstream wave T and u are below the ambient while $T > 1$ and $u < u_0$ for the upstream wave. After both waves leave the domain all that remains is the equilibrium solution. This is compared to the exact solution computed from (50) and (51) in Figs. 9 and 10. Clearly the correctness of this aspect of the computation has been established, for example, the maximum error of u in Fig. 10 is 4.9474×10^{-4}.

The first few images in Fig. 8 show that in response to the sudden appearance of the constriction, u initially decreases in front of it, though later, in equilibrium, this deficit is gone. Fig. 11 containing the corresponding time history of θ shows that the initial slow down in u is a compressive motion (with $\theta < 0$) that is the initial basis for the upstream traveling wave. In effect, information about the presence of the constriction travels upstream at speed $u - \sqrt{T}$, leaving in its wake the ensuing equilibrium flow in which the fluid expands as it approaches the constriction and contracts upon passing it. A similar commentary applies to the downstream moving wave created by the sudden appearance of the constriction, except that its leading edge is seen from Fig. 11 to be an expansion of the fluid, followed by a compression.

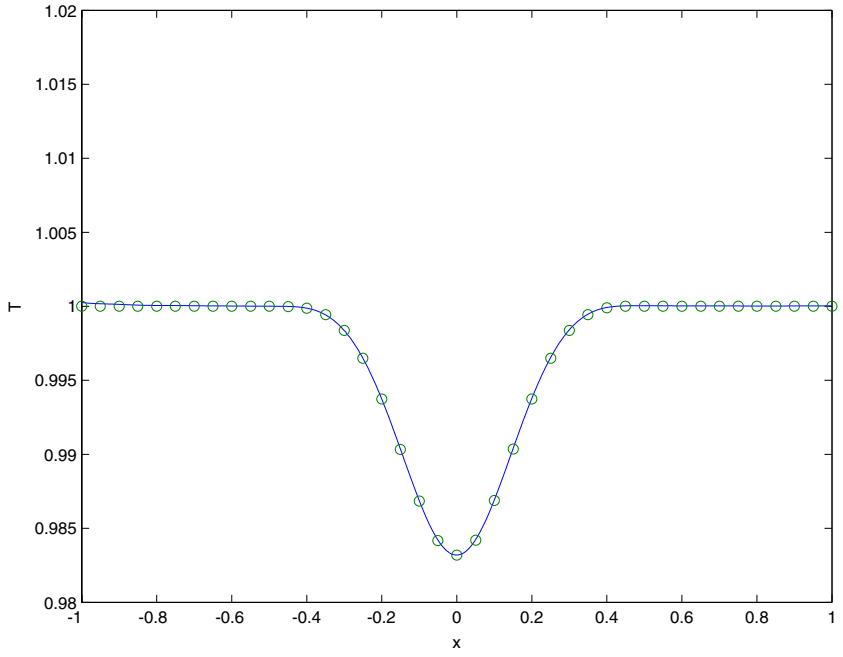

Fig. 9. Comparison of computed T (—) with exact solution (○).

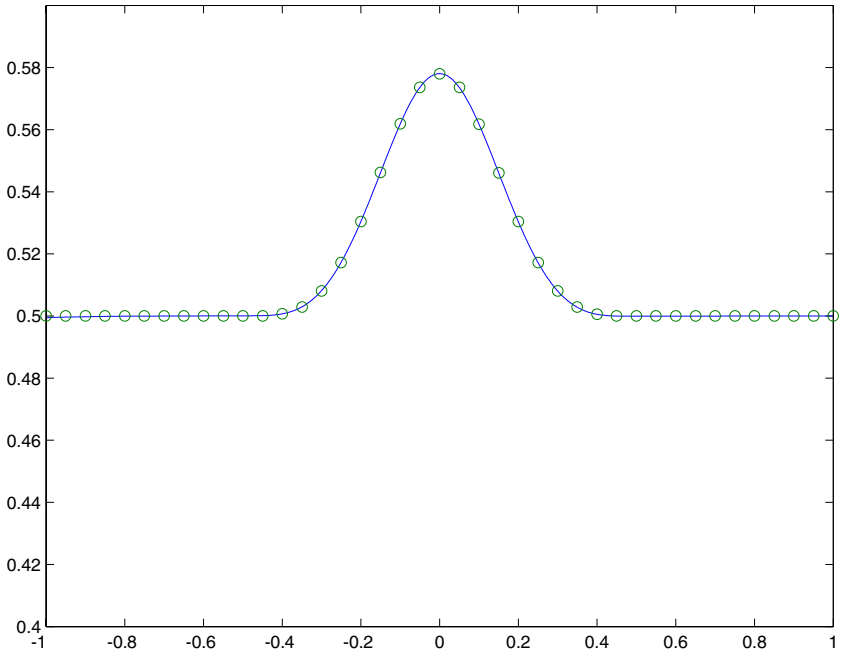

Fig. 10. Comparison of computed u (—) with exact solution (○).

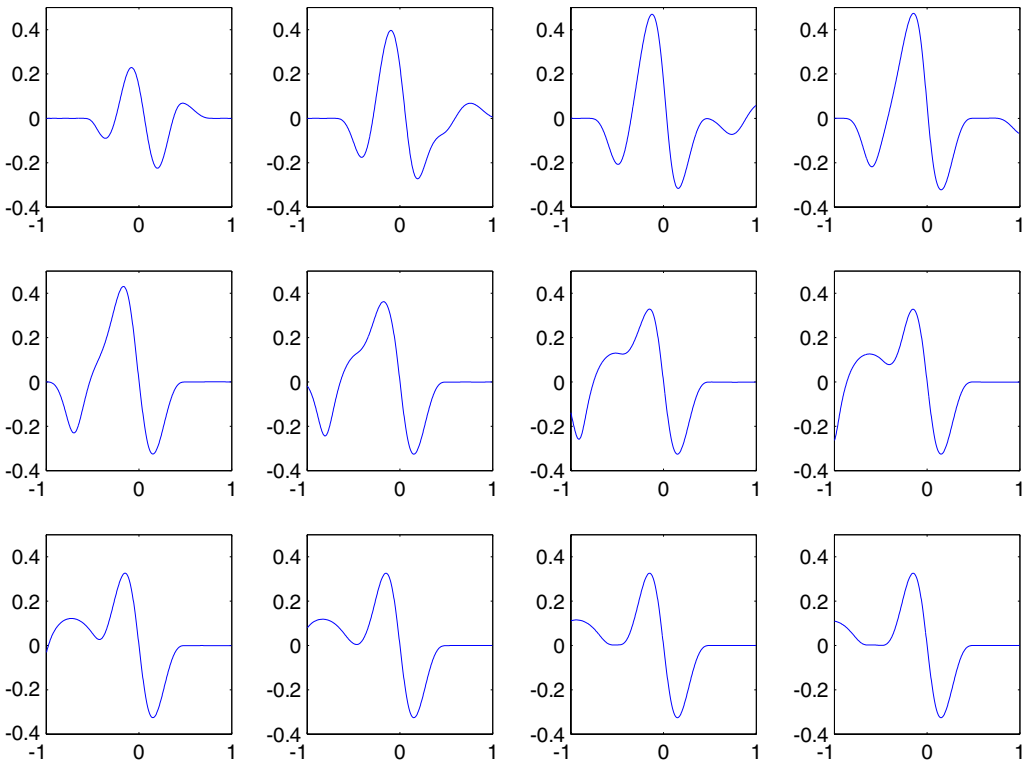

Fig. 11. θ in increments of 0.2 from $t = 0.2$ to 2.4 (left to right and top to bottom) for $u_0 = 0.5$ solution.

The equilibrium θ field for $u_0 = 0.5$ is compared to the quasi-1D incompressible θ given by (6) in Fig. 12. At this Mach number there is clearly a significant additional compression/expansion associated purely with compressibility.

A different perspective on the transient solution is given in Figs. 13–16 giving T, u, θ, and $\partial^2 T/\partial x^2$, respectively, at equally spaced time intervals for a solution with $u_0 = 0.4$ on the larger region $|x| \leqslant 1.5$. The constancy of the maxima and minima of T and u in the waves is shown in Figs. 13 and 14. On the other hand, the θ plot in Fig. 15 reveals a steepening of the wave front associated with the upstream compressive wave while the trailing rarefaction has diminishing amplitude. A relatively short distance further up the duct the left-moving wave will develop a shock with temperature jump given by the difference between the upstream ambient and the maximum of T and a jump in velocity from u_0 to its minimum. Behind the shock the flow relaxes back to the ambient condition. The leading edge of the right traveling wave is a rarefaction that spreads slowly while its trailing edge steepens. These features are also evident in Fig. 15.

Since the present scheme is not designed to model shocks and the upstream wave is progressing rapidly toward a singularity, there is clearly a limit on how far upstream x_l can be chosen. In fact, even before the appearance of the shock, the compression of the flow leads to an exceedingly rapid variation in T that is strongly reflected in $\partial^2 T/\partial x^2$ as seen in Fig. 16. For example, in the short distance from -1 to -1.5 the magnitude of $\partial^2 T/\partial x^2$ increases by approximately 40%, placing great demands on resolution and the least-square fit. Computations show that if there is insufficient elements to resolve the details of T including its second derivative, spurious waves are likely to develop that cause instability, mainly in the form of high frequency waves that pass through the boundary causing unphysical changes to Δ_l and Δ_r that induce

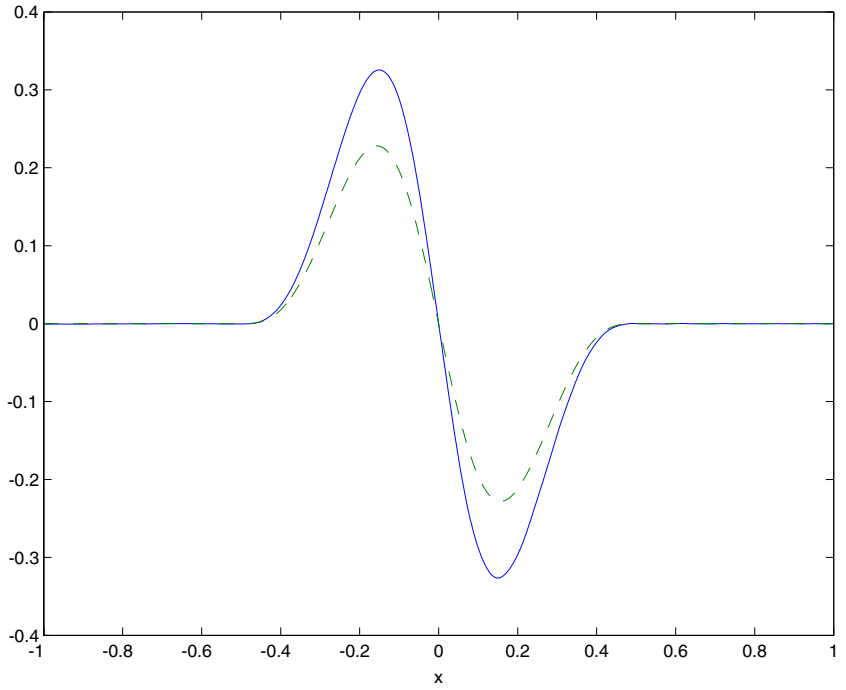

Fig. 12. Equilibrium θ distribution (—) compared to the quasi-1D incompressible distribution (6) (- - -).

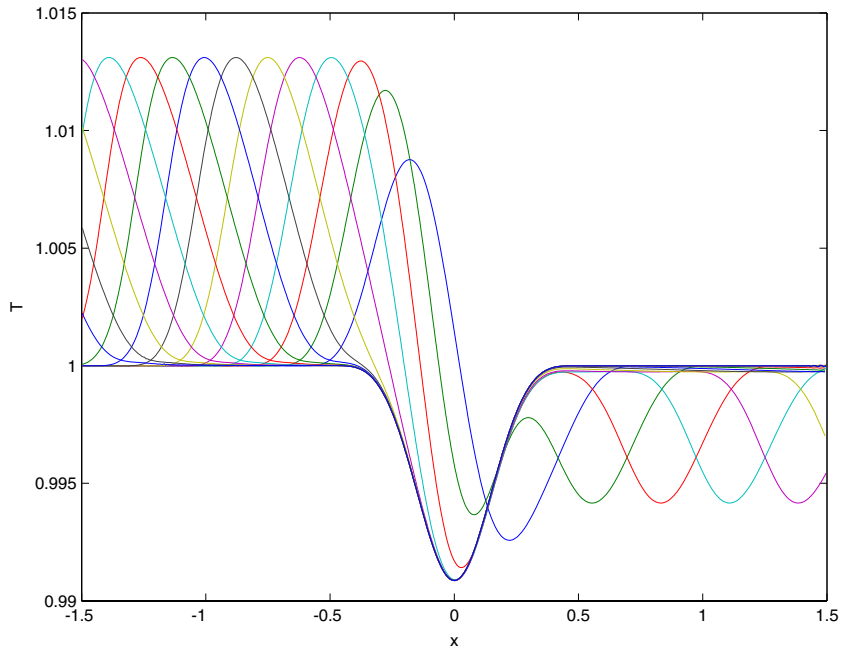

Fig. 13. T at time increments of 0.2 for $t = 0.2$ to 3.0 for $u_0 = 0.4$.

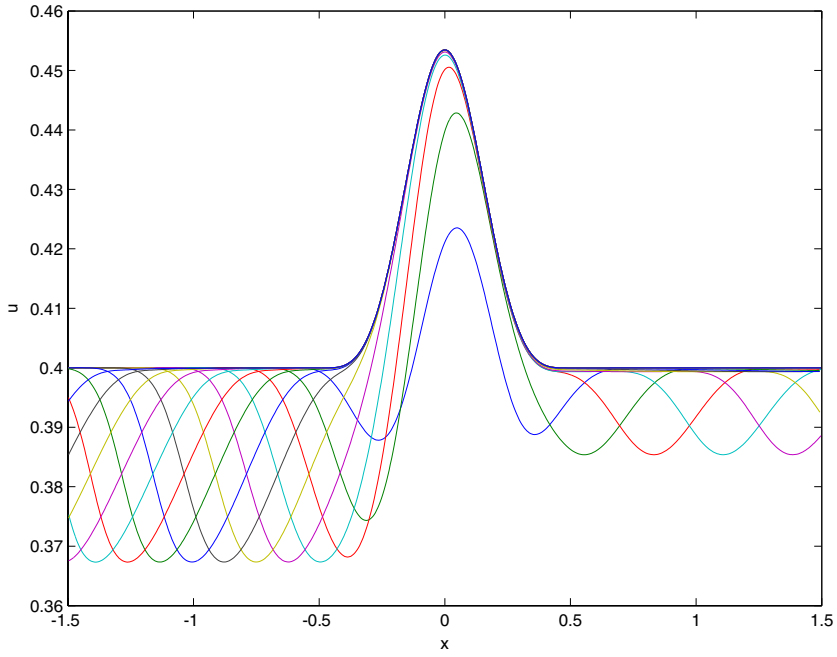

Fig. 14. u at time increments of 0.2 for $t = 0.2$ to 3.0 for $u_0 = 0.4$.

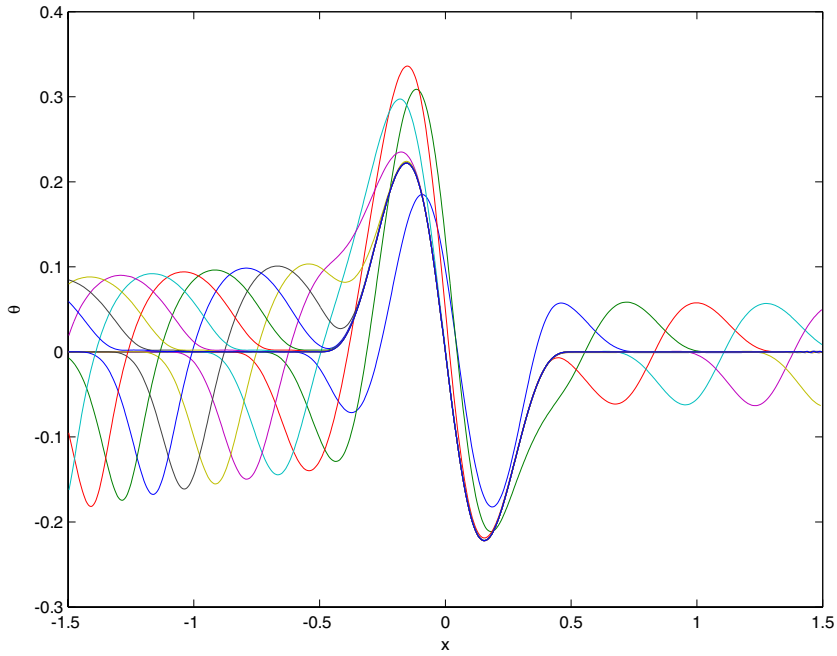

Fig. 15. θ at time increments of 0.2 for $t = 0.2$ to 3.0 for $u_0 = 0.4$.

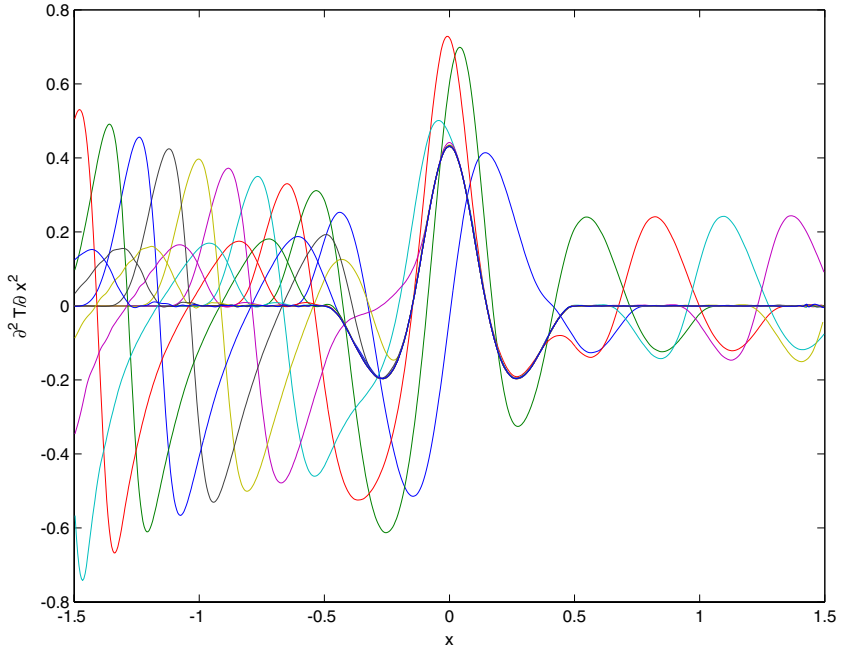

Fig. 16. $\partial^2 T/\partial x^2$ at time increments of 0.2 for $t = 0.2$ to 3.0 for $u_0 = 0.4$.

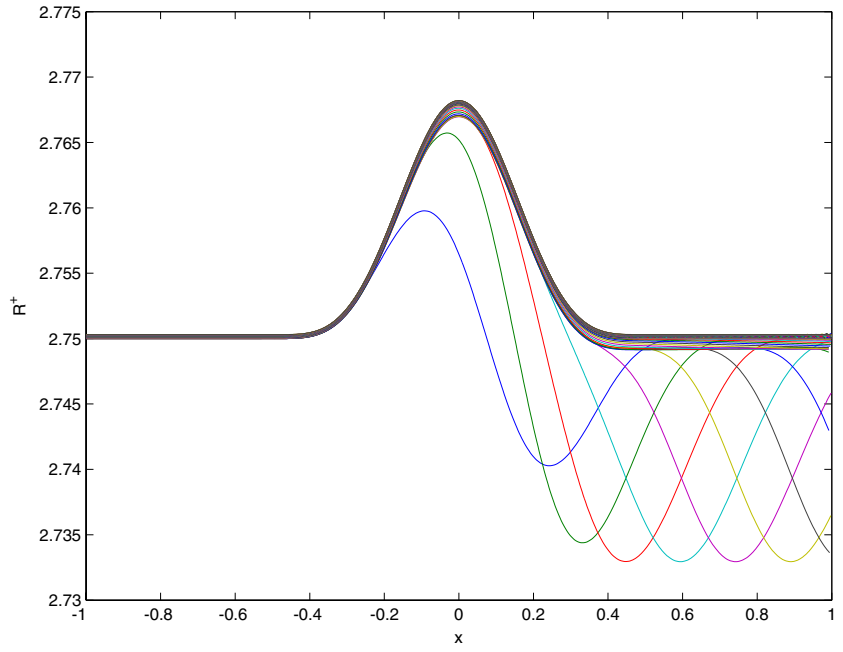

Fig. 17. Constancy of (28) on left moving characteristics.

further waves and so on. As a general rule, the resolution required for $\partial^2 T/\partial x^2$ in the upstream wave is much more restrictive than that required in the equilibrium solution through the nozzle and this is therefore the pacing item that determines an acceptable flow resolution.

According to our previous analysis of the boundary conditions, (28) should have a constant common value for the waves on the left side of the constriction that are traveling toward the inflow boundary, while (29) should be uniformly constant for the waves traveling on the right side of the constriction toward the outflow boundary. Figs. 17 and 18 are plots of the respective Riemann invariants for the same data as in Figs. 7–11. These conform to the expected behavior in which $R^+ = 2.75$ and $R^- = -2.25$ thus helping to validate the physicality of this aspect of the solution.

Another interesting aspect of the computations is the behavior of h. Fig. 19 contains a space–time contour plot of h for the solution with $u_0 = 0.5$. Vertical lines give a view of the h distribution among the elements at a fixed time. The transient behavior of h can be reconstructed by regarding the figure from left to right. Dashed and solid contours signify h below and above the nominal value $\overline{h}$, respectively. According to the figure, it takes considerably longer, until $t \approx 6.5$, for equilibrium to be established in this case than it does for the other variables in Figs. 7, 8 and 11. Among the phenomena is a slight rise in h that travels rapidly downstream with the main wave, followed by a deficit in h that moves downstream at essentially the convection velocity. Moving upstream with the principal wave from the constriction is a region of small h. When this disturbance reaches x_l at approximately $t = 2$, it appears to reflect off the boundary in the form of a wave of $h > \overline{h}$ that travels downstream the length of the domain from x_l to x_r at the convection speed. This wave temporarily disturbs the h equilibrium that had already formed in the constriction region before passing through and leaving the computational domain at the downstream boundary. The end result is an equilibrium with the dilatation elements stretching as they approach the constriction and contracting back to their original length as they depart.

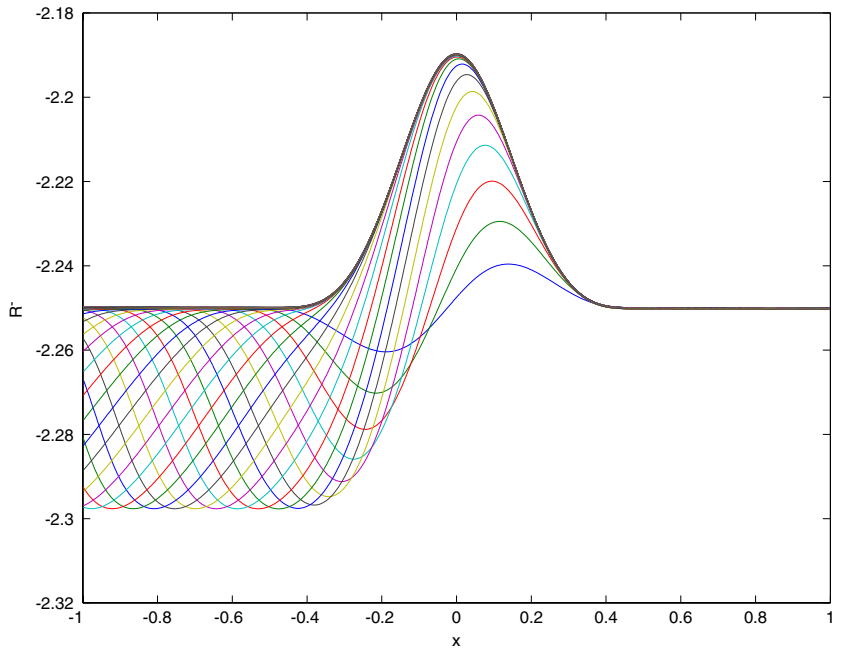

Fig. 18. Constancy of (29) on right moving characteristics.

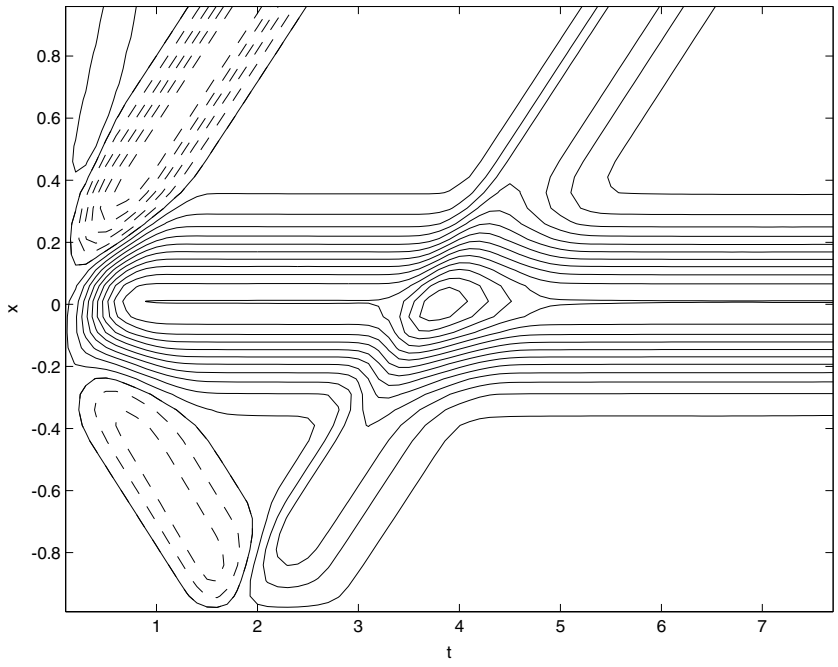

Fig. 19. Space–time contour of h. Dashed contours are $h < \overline{h}$ and solid contours are $h \geqslant \overline{h}$.

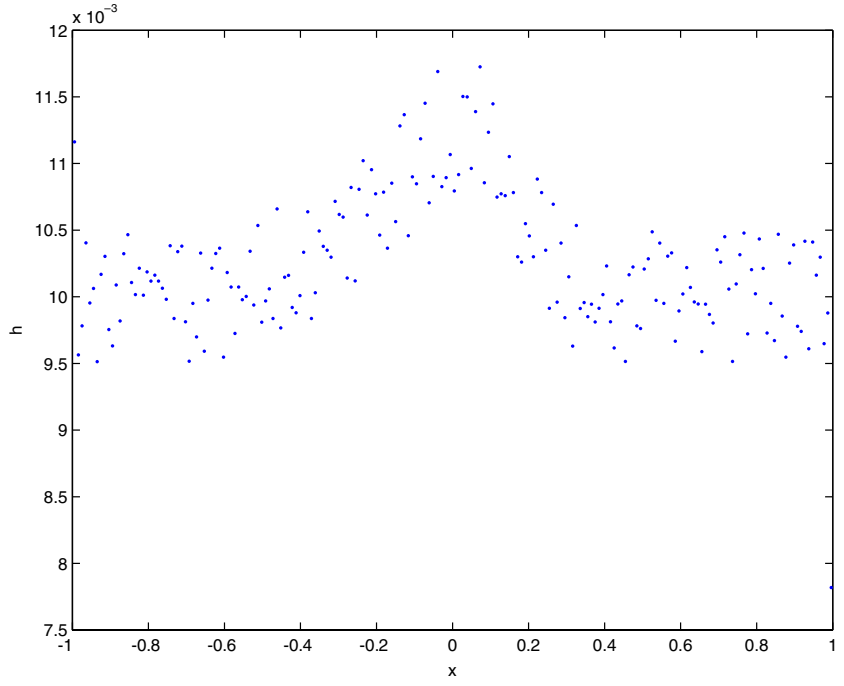

Fig. 20. Non-uniform h distribution.

Computations were also done in which the domain was initially divided into randomly sized elements, and kept this way for all time by randomly varying the size of the incoming elements at the upstream boundary. A typical distribution of element lengths for one such computation is shown in Fig. 20. In fact, the predicted u and T fields associated with this solution are indistinguishable from those in Figs. 9 and 10 based on more uniformly sized elements. This result is consistent with the observations of Marshall and Grant in a related context [16] and suggests that the least-square algorithm used in this work, after appropriate generalization, may also succeed in the context of three-dimensional, turbulent flow.

Another test of the accuracy of the algorithm, including how well the velocity field is evaluated, is given by examining the degree to which the computed solutions are consistent with the identity (17). In fact, using the definitions of Δ_l and Δ_r this leads to the approximation

$$0 = \Delta_l + \sum_{i=1}^{N} h_i \theta_i + \Delta_r, \tag{52}$$

where the sum is over the elements in the computational domain. Some idea of how well the computed solution for the case with $u_0 = 0.5$ satisfies (52) is given in Fig. 21. It is seen that the sum of the three terms remains very small despite the passage of the waves through the boundaries. First, while the right moving wave passes through x_r beginning at approximately $t = 0.5$, the sum over interior elements balances with Δ_r. Later, at $t = 1.5$ it balances with Δ_l as the left moving wave travels through the inflow boundary. In essence this figure shows the successful transfer of θ between the computational domain and the exterior region. Note that prior to the first wave reaching a boundary, the sum of terms in (52) can only be non-zero due to the summation term. According to the figure this source of error is quite small. Finally, after each wave has left the domain, Δ_l and Δ_r should be zero to reflect the fact that their integrated dilatation makes no contribution to velocity in the computational region. Indeed this criterion is seen also to be well met.

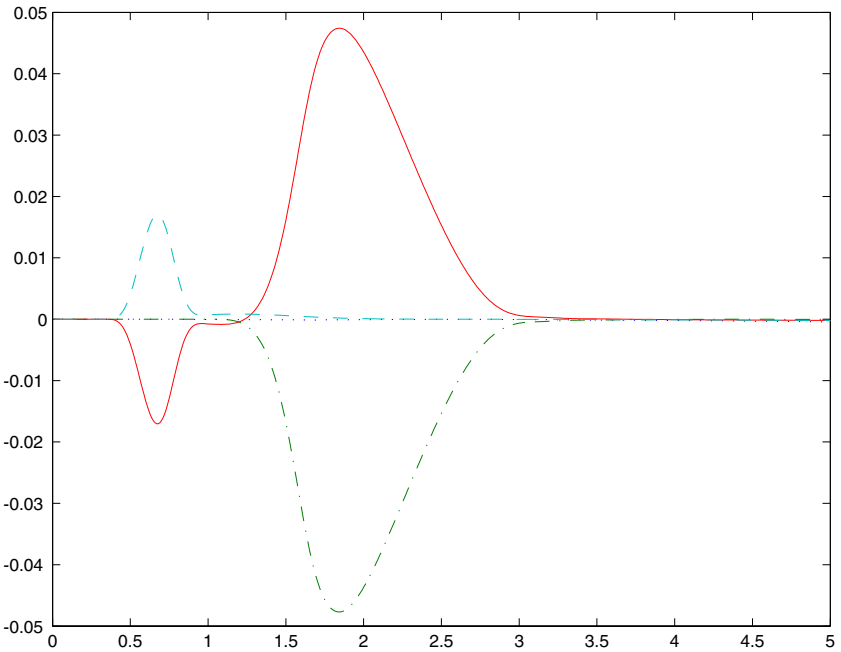

Fig. 21. Decomposition in (52) as a function of time for the solution with $u_0 = 0.5$. - · -, Δ_l; —, $\sum_{i=1}^{N} h_i$; - - -, Δ_r; · · ·, sum of terms.

6. Conclusions

A grid-free scheme for solving quasi-one dimensional, isentropic, compressible flow has been derived and shown to work well in the solution of subsonic compressible flow through a constricted duct. An essential aspect of this work is the treatment of inflow and outflow boundary conditions using the wave properties of the 1D gas dynamics equations. These had to accommodate the need for data sets with which to do least square fitting of the temperature field at points adjacent to the boundaries as well as allow for the passage of dilatation carried by waves without significant distortion or reflection back into the flow. Left for future work is how to best maintain resolution of compression waves that develop into shocks as they move into the undisturbed fluid.

The present scheme has been developed with a view to its extension to 3D flows. In the latter case the velocity will be recovered from a sum over the contributions from individual dilatation elements according to 3D potential flow formulas. There will, in addition, be velocities due to vortex elements. We expect that least-square fitting in 3D should be feasible [10] though techniques that accelerate the process may be necessary if the number of elements is large. Generalization of the present technique for accommodating the inflow and outflow boundary conditions to 3D represents an interesting aspect of future work. It is also desirable in the interest of efficiency to equip the 3D analogue of this approach with a capability for adding and subtracting dilatation elements where necessary.

Acknowledgements

This material is based in part upon work supported by an ATP/NIST award to VorCat, Inc. Computer time was provided in part by NCSA.

References

[1] J.D. Anderson Jr., Computational Fluid Dynamics, McGraw-Hill, New York, 1995.
[2] P.S. Bernard, A deterministic vortex sheet method for boundary layer flow, J. Comp. Phys. 117 (1995) 132–145.
[3] P.S. Bernard, J.P. Collins, J. Krispin, Gridfree simulation of turbulent boundary layers using VorCat, in: 16th AIAA Computational Fluid Dynamics Conference, Orlando, FL, 2003, AIAA Paper No. 2003-3424.
[4] P.S. Bernard, M.A. Potts, J. Krispin, Studies of turbulent mixing using the VorCat implementation of the 3D vortex method, in: 33rd AIAA Fluid Dynamics Conference, Orlando, FL, 2003, AIAA Paper No. 2003-3599.
[5] A.J. Chorin, Hairpin removal in vortex interactions II, J. Comput. Phys. 107 (1993) 1–9.
[6] G.H. Cottet, S. Mas-Gallic, A particle method to solve the Navier–Stokes system, Numer. Math. 57 (1990) 805–827.
[7] J.D. Eldredge, T. Colonius, A. Leonard, A dilating vortex particle method for compressible flow, J. Turbul. 3 (2002), Art. No. 036.
[8] J.D. Eldredge, T. Colonius, A. Leonard, A vortex particle method for two-dimensional compressible flow, J. Comput. Phys. 179 (2002) 371–399.
[9] A.F. Ghoniem, A.J. Chorin, A.K. Oppenheim, Numerical modeling of turbulent flow in a combustion tunnel, Phil. Trans. Roy. Soc. 304 (1982) 303–325.
[10] A.A. Gossler, Moving least squares: a numerical differentiation method for irregularly spaced calculation points, Sandia National Laboratories Report SAND 2001-1669, 2001.
[11] S.E. Guarini, R.D. Moser, K. Shariff, A. Wray, Direct numerical simulation of a supersonic turbulent boundary layer at Mach 2.5, J. Fluid Mech. 414 (2000) 1–33.
[12] R. Lechner, J. Sesterhenn, R. Friedrich, Turbulent supersonic channel flow, J. Turbul. 2 (2001), Art. No. 001.
[13] E. Lenormand, P. Sagaut, L.T. Phuoc, Large eddy simulation of subsonic and supersonic channel flow at moderate Reynolds number, Int. J. Numer. Meth. Fluids 32 (2000) 369–406.
[14] T. Maeder, N.A. Adams, L. Kleiser, Direct simulation of turbulent supersonic boundary layers by an extended temporal approach, J. Fluid Mech. 429 (2001) 187–216.
[15] J.R. Mansfield, O.M. Knio, C. Meneveau, Dynamic LES of colliding vortex rings using a 3D vortex method, J. Comput. Phys. 152 (1999) 305–345.

[16] J.S. Marshall, J.R. Grant, A Lagrangian vorticity collocation method for viscous, axisymmetric flows with and without swirl, J. Comput. Phys. 138 (1997) 302–330.
[17] M. Nitsche, J.H. Strickland, Extension of the gridless vortex method into the compressible flow regime, J. Turbul. 3 (2002), Art. No. 001.
[18] E.G. Puckett, Vortex methods: an introduction and survey of selected research topics, in: M.D. Gunzburger, R.A. Nicolaides (Eds.), Incompressible Computational Fluid Dynamics: Trends and Advances, Cambridge University Press, Cambridge, 1993, pp. 335–407.
[19] J.H. Strickland, Gridless compressible flow: a white paper, Sandia National Laboratory Report SAND2001-057, 2001.
[20] L. Tang, C.T. Crowe, J.N. Chung, T.R. Troutt, A numerical model for droplets dispersing in a shear layer including coupling effects, ASME FED 91 (1990) 27–34.